

Atomistic Simulation of the Rate-Dependent Ductile-to-Brittle Failure Transition in Bicrystalline Metal Nanowires

Weiwei Tao,[†] Penghui Cao,[‡] and Harold S. Park^{*,†}

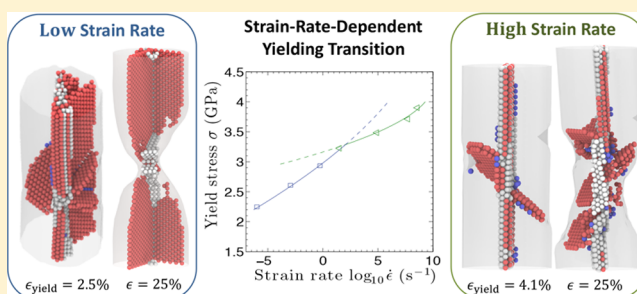
[†]Department of Mechanical Engineering, Boston University, Boston, Massachusetts 02215, United States

[‡]Department of Nuclear Science and Engineering, Massachusetts Institute of Technology, Cambridge, Massachusetts 02139, United States

Supporting Information

ABSTRACT: The mechanical properties and plastic deformation mechanisms of metal nanowires have been studied intensely for many years. One of the important yet unresolved challenges in this field is to bridge the gap in properties and deformation mechanisms reported for slow strain rate experiments ($\sim 10^{-2}$ s $^{-1}$), and high strain rate molecular dynamics (MD) simulations ($\sim 10^8$ s $^{-1}$) such that a complete understanding of strain rate effects on mechanical deformation and plasticity can be obtained. In this work, we use long time scale atomistic modeling based on potential energy surface exploration to elucidate the atomistic mechanisms governing a strain-rate-dependent incipient plasticity and yielding transition for face centered cubic (FCC) copper and silver nanowires. The transition occurs for both metals with both pristine and rough surfaces for all computationally accessible diameters (< 10 nm). We find that the yield transition is induced by a transition in the incipient plastic event from Shockley partials nucleated on primary slip systems at MD strain rates to the nucleation of planar defects on non-Schmid slip planes at experimental strain rates, where multiple twin boundaries and planar stacking faults appear in copper and silver, respectively. Finally, we demonstrate that, at experimental strain rates, a ductile-to-brittle transition in failure mode similar to previous experimental studies on bicrystalline silver nanowires is observed, which is driven by differences in dislocation activity and grain boundary mobility as compared to the high strain rate case.

KEYWORDS: Bicrystalline metal nanowire, ductile-to-brittle transition, incipient plasticity and yielding transition, self-learning metabasin escape algorithm



The mechanical properties and failure mechanisms of metal nanostructures have been studied intensely for many years. This has been partly due to the significant potential of these materials across a range of nanotechnology applications,^{1,2} and partly as a basic scientific question to uncover how and why their mechanical properties change as their characteristic sizes are reduced to nanometer dimensions.^{3–7}

Insights into the mechanical properties and plastic deformation mechanisms of metal nanowires have been obtained through both classical molecular dynamics (MD) simulations,^{4,5,8–12} as well as nanomechanical experiments.^{6,7,13–23} However, as is well-known, MD simulations operate at time scales (micro- to nanoseconds) and strain rates ($\dot{\epsilon} = 10^6$ – 10^9 s $^{-1}$) which are almost 10 orders of magnitude different from experimentally-relevant time scales (seconds or longer) and strain rates ($\dot{\epsilon} = 10^{-4}$ – 10^0 s $^{-1}$). This can lead to discrepancies in understanding of nanowire plasticity at different time scales, particularly if the incipient plastic deformation mechanism is strain-rate-dependent, as in the recent experiments of Ramachandramoorthy et al.²² and slow strain rate simulations by Yan and Sharma.²⁴ In particular, an implicit assumption in studying nanowire plasticity has been to

assume that similar defect nucleation mechanisms are observed at all strain rates,^{12,22} which could lead to inaccurate predictions in the energetic barriers to defect nucleation, the inability to capture strain-rate-sensitive plasticity transitions, and errors in predicting the yield stress as the strain rate decreases.

In this work, we present direct observations, using atomistic simulation techniques that can access long time scales and slow strain rates,²⁵ of strain-rate-dependent transitions in the incipient plastic deformation mechanisms, yield stress, and finally ductile-to-brittle failure mechanism for ultrasmall (diameter < 10 nm) bicrystalline metal nanowires. These results are distinct in focus from most experimental studies, which have typically centered on size and microstructure effects on the mechanical properties and plasticity of nanowires.^{4,6,7,26,27} They are also distinct from previous MD simulations and experiments that studied the effects of internal microstructure (grain and twin boundaries (TBs)) on the mechanical properties of nanowires^{23,28–32} because we demonstrate how

Received: November 24, 2017

Revised: December 21, 2017

Published: January 3, 2018

the plastic deformation mechanisms that nucleate from internal planar boundaries are strain-rate-dependent. Specifically, we find a strain-rate-dependent yield transition in both silver and copper bicrystalline nanowires, which is governed by the change in incipient plastic event from Shockley partials nucleated on primary slip systems at MD strain rates to the nucleation of planar defects on non-Schmid slip planes at experimental strain rates, where the incipient planar defect is the formation of multiple TBs for copper and stacking faults (SFs) for silver. Finally, we demonstrate that, at experimental strain rates, a ductile-to-brittle transition in failure mode similar to previous experimental studies on bicrystalline silver nanowires is observed,²² which is driven by differences in dislocation activity and grain boundary (GB) mobility as compared to the high strain rate case.

Brief Overview of SLME. While MD has led to many fundamental insights on the plasticity of nanomaterials and nanowires, it operates at time scales and strain rates that are significantly different from those seen in nanomechanical experiments.⁷ Because of this, we use in this work the recently developed self-learning metabasin escape (SLME) method^{25,33–35} to study the incipient defect nucleation and subsequent yield mechanisms for strain rates ranging from MD to experimental. We note that various other time-scaling approaches have been proposed for atomistics, and we refer the interested reader to more detailed discussions available in recent review papers.^{25,36–38} The SLME approach performs potential energy surface (PES) exploration using a modified, and more computationally efficient, version of the autonomous basin climbing (ABC) method originally proposed by Yip and co-workers.^{39–41} The key step is that a direct connection between energy barriers crossed on the PES and strain rate is made using transition state theory. In doing so, we have demonstrated the ability of the method to access slow, experimentally relevant strain rates and time scales leading to the discovery of new deformation mechanisms for systems such as amorphous solids^{34,35,42} and protein.^{43,44} An overview of the SLME method can also be found in a recent review paper.²⁵

For the SLME method, the connection between PES exploration and strain rate is through transition state theory. Specifically, we use an approach developed in previous SLME works^{34,35} by beginning with the following expression for strain rate, which was derived by Zhu et al. from transition state theory (TST) assuming constant temperature and strain rate¹²

$$\dot{\epsilon} = n\nu_0 \frac{k_B T}{E(\sigma, T) \Omega(\sigma, T)} \exp\left(-\frac{Q(\sigma, T)}{k_B T}\right) \quad (1)$$

where n is the number of independent nucleation sites, ν_0 is the attempt frequency, $E(\sigma, T)$ is the Young's modulus, $\Omega(\sigma, T)$ is the activation volume, and $Q(\sigma, T)$ is the activation free energy for dislocation nucleation. The activation free energy can be expressed as $Q(\sigma, T) = (1 - T/T_m) Q_0(\sigma)$, where T_m is the surface disordering temperature, and $Q_0(\sigma)$ is the activation energy on the zero temperature potential energy surface (PES).

By defining a characteristic prefactor $\dot{\epsilon}_0 = n\nu_0 \frac{k_B T}{E(\sigma, T) \Omega(\sigma, T)}$, we can rewrite eq 1 as

$$\dot{\epsilon} = \dot{\epsilon}_0 \exp\left(-\frac{(1 - T/T_m) Q_0(\sigma)}{k_B T}\right) \quad (2)$$

Bicrystalline Nanowires. In this work, we apply the SLME method to study the plastic deformation mechanisms in

bicrystalline silver and copper nanowires spanning about 10 orders of magnitude in strain rate, i.e., from high rate MD to experimental. We chose this nanowire system because it has recently been investigated both experimentally and using MD simulations,²² and also because we are interested in examining strain rate effects on the plastic deformation mechanisms that nucleate from internal planar boundaries.

To create the bicrystalline nanowires shown in Figure 1a, we followed the procedure described previously.²² Specifically, the

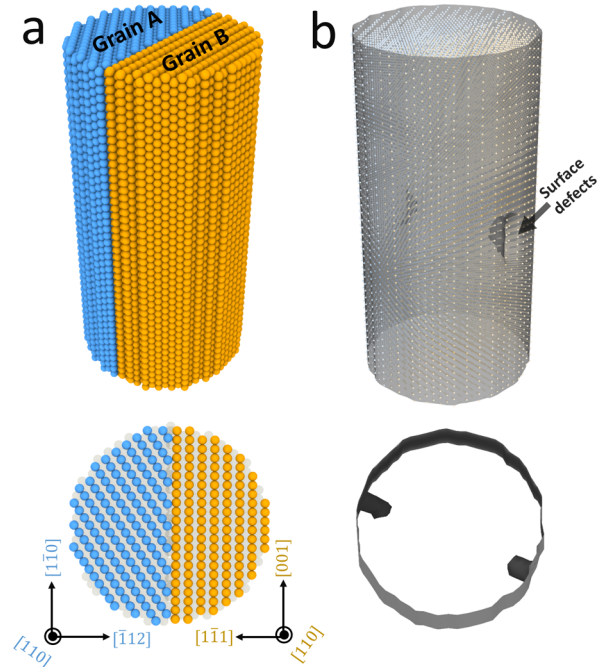


Figure 1. (a) Atomistic model of a pristine 4.5 nm diameter bicrystalline silver nanowire. Grain A (blue) and grain B (orange) follow the lattice directions shown in the bottom image, which results in the grains being tilted by 35.26° about the $[110]$ direction with respect to each other. (b) Surface configuration of the silver nanowire with surface roughness. Surface defects are introduced in the nanowire by removing selected atoms from the pristine configuration as described in the main text. Bottom images show atomic structure looking down the $[110]$ nanowire axis.

two grains are built following the lattice directions in Figure 1a, which results in grain A and grain B being tilted by 35.26° about the $[110]$ direction with respect to each other. Rigid body translations of one grain with respect to the other are used to sample a number of initial configurations.^{22,45,46} Because the grain rotation may cause atoms to be physically too close to each other within the GB, atoms that are closer than a critical distance of $0.25a_0$, where a_0 is the lattice constant, are removed from the system. Subsequently, a nanowire with circular cross section was cut out from the original simulation cell. Periodic boundary conditions are maintained along the nanowire axis while the transverse directions are free, creating free surfaces along the nanowire. We then performed conjugate gradient energy minimization to find a minimum energy configuration, where the configuration with the lowest potential energy was chosen for our study.⁴⁶

We also considered nanowires with surface roughness, similar to the experimentally studied bicrystalline silver nanowires of Ramachandramoorthy et al.²² Surface roughness was created in both grains of the bicrystalline nanowires by removing atoms

up to a depth of 0.8 nm with a roughness diameter of 1.5 nm in both grains. We will quantify the effect of surface roughness on the strain-rate-dependent incipient plasticity transitions later in this work.

Due to the computational expense of the SLME method, we perform simulations in this work on 4.5 and 6.5 nm diameter bicrystalline silver and copper nanowires with periodic boundary conditions along the nanowire axial direction, which enable us to bridge the gap in strain rates from MD to experimental, but do not allow us to perform a direct comparison to the experiments in size scale. Copper nanowires were modeled using the embedded atom method (EAM) interaction potential for copper developed by Mishin et al.,⁴⁷ while the silver nanowires were modeled using the EAM potential of Williams et al.,⁴⁸ which was also used by Ramachandramoorthy et al.²² The visualization of the nanowire deformation mechanisms was performed using the software OVITO.⁴⁹

Results. Benchmarking SLME Results against Classical MD at High Strain Rates. We first benchmark the SLME results against classical high strain rate MD simulations before using the SLME method at slower strain rates that are not accessible using MD. Figure 2 shows a comparison of the

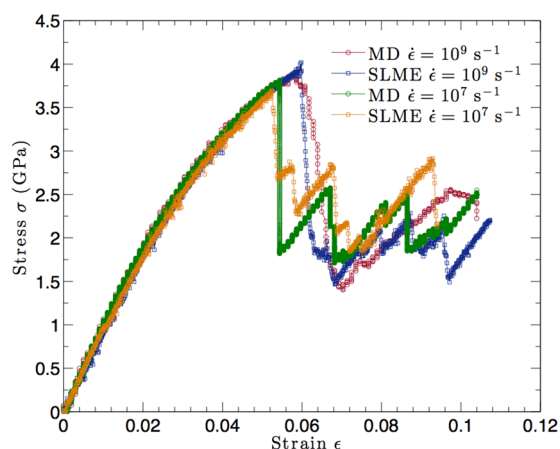


Figure 2. Validating SLME results against benchmark MD results for stress–strain curves at two different high strain rates of $\dot{\epsilon} = 10^9 \text{ s}^{-1}$ and $\dot{\epsilon} = 10^7 \text{ s}^{-1}$ at a temperature of 300 K for 4.5 nm bicrystalline silver nanowires with pristine surfaces.

SLME and MD-generated stress–strain curves at room temperature for the MD-accessible strain rate of $\dot{\epsilon} = 10^9 \text{ s}^{-1}$ and $\dot{\epsilon} = 10^7 \text{ s}^{-1}$ for 4.5 nm bicrystalline silver nanowires with pristine surfaces. To calculate the stress–strain response for a prescribed constant strain rate, we used the method previously developed by Cao et al.,^{34,35} as detailed in the Supporting Information.

The Young's modulus for this bicrystalline silver nanowire is 104.5 GPa at a strain rate of 10^9 s^{-1} , which is comparable to the reported Young's modulus of 112.4 GPa for a 4.4 nm square cross section $\langle 110 \rangle$ -oriented silver nanowire.⁵⁰ The modulus does not change appreciably when the strain rate decreases to 10^7 s^{-1} , while the yield strain decreases from 6% to 5.3%, and the yield stress decreases from 3.95 to 3.7 GPa by reducing the strain rate from 10^9 to 10^7 s^{-1} . We note that the yield stress as defined here and throughout this paper corresponds to when a large drop in stress is observed, as clearly seen at the different strain rates in Figure 2. The SLME results match the MD

results for both the Young's modulus, and also the yield strain and yield stress, as well as the general postyield behavior, including the large stress drop after yield that is characteristic of nanowires that are subject to displacement-controlled loading.²²

SLME Investigation of Stress and Strain-Rate-Dependent Incipient Plastic Deformation Mechanisms. We now present and discuss the key results of this investigation, i.e., the strain-rate-dependent transition in incipient plastic deformation mechanisms for face centered cubic (FCC) metal bicrystalline nanowires. We find the mechanical properties of the bicrystalline nanowires share some common features at different strain rates as shown in Figure 2. In particular, while the yield stress varies with strain rate, the elastic modulus, and thus the elastic pathway traversed by the nanowire before yielding, is quite similar. We exploit this feature by considering different dislocation free structures for various stress states prior to yielding. At each of these stress states, the SLME approach is utilized to explore the PES while the nanowire length is held fixed until yielding of the nanowires is observed.

Figure 3 shows results for 4.5 nm diameter bicrystalline silver and copper nanowires with pristine surfaces immediately after yielding at different stress levels. Later, we will connect these

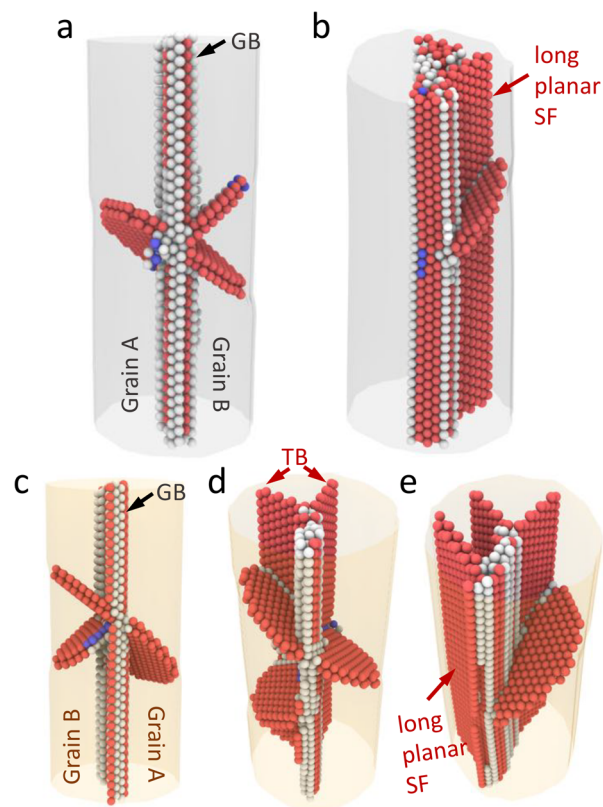


Figure 3. Atomic configurations immediately after yielding from SLME simulations at stresses of (a) 3.9 and (b) 2.2 GPa for bicrystalline silver nanowires with pristine surfaces and diameter of 4.5 nm. Atomic configurations immediately after yielding from SLME simulations at stresses of (c) 5.23, (d) 4.29, and (e) 3.06 GPa for bicrystalline copper nanowires with pristine surfaces and diameter of 4.5 nm. In all cases, yielding, which is defined by a significant drop in stress, is caused by the emission of partial dislocations on primary slip planes. Only planar defects are visualized. The following color convention is used in all images in this figure: gray planes, GB; single red plane, TB; two adjacent red planes, SF.

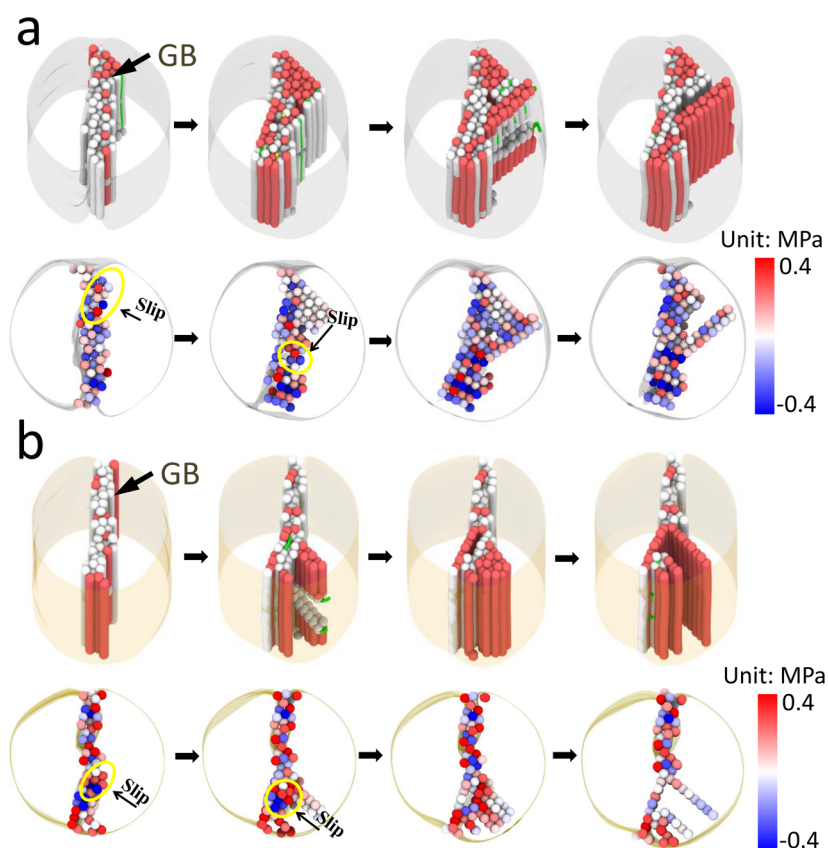


Figure 4. (a) (top) Atomic configurations and (bottom) atomic shear stress distribution before and after the formation of long, planar SFs at a stress of 2.6 GPa for 4.5 nm bicrystalline silver nanowires with pristine surfaces. These SFs correspond to that shown in Figure 3b. (b) (top) Atomic configurations and (bottom) atomic shear stress distribution before and after the formation of the TBs at a stress of 3.06 GPa for 4.5 nm bicrystalline copper nanowires with pristine surfaces. These TBs correspond to that shown in Figure 3d,e. For both parts a and b, top images are colored by the dislocation extraction algorithm (DXA) in OVITO while the bottom images are colored by atomic shear stress with color bar shown on the image. The atomic shear stress is calculated as described in the Supporting Information. The arrows in bottom images point to the nucleation point for Shockley partial dislocations. Only the GB and other planar defects are visualized. Single red plane, TB; two adjacent red planes, SF; green line, Shockley partial dislocation.

stress levels to their corresponding strain rates via eq 2 to demonstrate that the transition in incipient plastic deformation mechanism seen in Figure 3 occurs at experimentally relevant strain rates.

Figures 3a,b illustrates the two different stress-dependent configurations we observed immediately after yielding for the silver nanowires. In the high stress regime ($\sigma > 3.2$ GPa), the incipient plastic event corresponds to the yielding event, which occurs via the nucleation of leading partials from the nanowire GB as shown in Figure 3a and Video S1. When these partials sweep through the grain, more dislocations are triggered and nucleated in the opposite grain. These dislocations glide along the (111) and (11 $\bar{1}$) slip planes with a Schmid factor of 0.471, which is in agreement with the MD simulations of Ramachandramoorthy et al., in which the same types of partials were observed in bicrystalline silver nanowires.²² We note that all yielding events nucleate from the nanowire surfaces if either surface roughness is present, or if larger diameter nanowires are considered as shown in the Supporting Information, Figure S4.

However, when the nucleation stress is below 3.2 GPa, a different sequence of plastic deformation events is observed prior to yielding in the bicrystalline silver nanowires, as shown in Figure 3b and Video S2. Specifically, Shockley partial dislocations are successively emitted on ($\bar{1}11$) and (1 $\bar{1}1$) slip planes from the GB. These partial dislocations then glide along

the slip direction, leaving several long, planar SFs. These SFs are particularly interesting because, unlike in the high stress cases, the slip plane on which the partial dislocations propagate has a zero Schmid factor, and as a result, the formation of these SFs does not cause yielding. Yielding subsequently occurs via the nucleation of leading partial dislocations as observed in the high stress cases.

In order to explore whether a similar stress-dependent transition in the incipient plastic event occurs in other FCC metal nanowires, we performed similar simulations for bicrystalline copper nanowires, as shown in Figure 3c–e. At high stresses ($\sigma > 4.5$ GPa), as illustrated in Figure 3c and Video S3, the first defect, which corresponds to the yielding event, is the same as the bicrystalline silver nanowires, i.e., dislocations gliding along the (111) and (11 $\bar{1}$) slip planes. However, when the stress is decreased, TBs are formed on slip planes with zero Schmid factor before yielding of the nanowire occurs as shown in Figure 3d and Video S4. We note that the same mechanism is also observed at constant strain rate simulations at a strain rate of 0.1 s⁻¹ prior to yielding of the nanowire as shown in Figure S1c and Video S5.

If the nucleation stress is lower (less than 3.7 GPa), after the emission of multiple TBs a long, planar SF on the ($\bar{1}11$) slip plane is emitted from the GB in grain B as illustrated in Figure 3e and Video S6. Yielding subsequently occurs via the gliding of

partial dislocations on primary slip planes from the free surface near the intersection between either the GB or the TBs and the surface. We note that the stresses in the bicrystalline copper nanowires are larger than those seen in the bicrystalline silver nanowires. This is expected due to the lower energetic cost for defect nucleation in silver as compared to copper.⁵¹

The formation of long, planar SFs in bicrystalline silver nanowires as well as multiple TBs in bicrystalline copper nanowires at low stresses prior to yielding share some common features as all of these planar defects occur on slip planes with zero Schmid factor; i.e., there is no resolved shear stress on the slip planes due to external loading. While a slip plane with a zero Schmid factor is one on which slip is unlikely to occur, this construct may not hold when the effects of the nearby GB are considered. Specifically, the GB can serve as a dislocation source due to the local stress fields resulting from the large numbers of disordered atoms it contains.

To demonstrate this, we plot in Figure 4 the defect nucleation processes for 4.5 nm diameter bicrystalline silver and copper nanowires with pristine surfaces before yield, and the corresponding atomic shear stress distribution along the slip direction on slip planes with zero Schmid factor as described in the Supporting Information. In Figure 4a, the top images show that successive partial dislocations are nucleated from the GB, where the green lines indicate the positions of the Shockley partial dislocations. The bottom images of Figure 4a show that dislocations nucleate from regions of the GB where atoms with a large positive stress value along the slip direction are next to atoms with a large negative value, as indicated in the circle. The nucleation of partial dislocations from these regions helps to relieve the local stress heterogeneity. This finding parallels with that of Yamakov et al.,⁵² who reported via MD simulation studies of the deformation of nanocrystalline FCC metals that the nucleation of partial dislocations is induced by the local shear stress regardless of the Schmid factor on the slip directions.

The nucleation process in copper as illustrated in Figure 4b is similar to that for silver. The partial dislocations are nucleated from the GB where a large stress heterogeneity exists. After the emission of two SFs, a trailing partial is nucleated on one of the slip planes that already contains a SF, then propagates and replaces a SF with a full dislocation, which leaves the configuration with several TBs. This TB formation process enables the reorganization of the lower portion of the GB, which divides the nanowire into three grains with different lattice directions. The newly formed grain C has a tilt angle of 73.5° with respect to grain B and an angle of 71.3° with respect to grain A about the [110] direction. The TBs that form therefore remove part of the less stable GB structure that was initially formed between grains A and B, which leads to the significant decrease in potential energy as shown in Figure S1b.

We also examined the effect of surface roughness, due to reports that the bicrystalline nanowires studied experimentally²² contained surface undulations. To do so, we introduced surface undulations to both the silver and copper bicrystalline nanowires as shown previously in Figure 1, and performed SLME simulations at different stress levels. For the materials and nanowire diameters we investigated, surface roughness did not impact the incipient nucleation mechanism transition as shown in Figure S2, and instead only impacted the energy barrier needed for the incipient mechanism, as discussed in the next section. Furthermore, due to the stress concentrations created by the surface undulations, the yielding dislocations on

primary slip planes were emitted from the regions of surface roughness at all strain rates. Finally, size effects were investigated by considering 6.5 nm diameter bicrystalline silver and copper nanowires. While the same transition in incipient deformation mechanism with decreasing stress was observed as previously described, as shown in Figure S3, we note that this transition may be size-dependent. This is because larger nanowires would incur a larger energetic penalty having twins or stacking faults nucleate along its loading axis than the smaller diameter nanowires studied computationally here.

Connecting the Nucleation Mechanism, Activation Energy, and Strain Rate. The SLME simulations have demonstrated that different incipient plastic deformation mechanisms prior to yielding are operant depending on the stress that is applied. However, at all stress levels, the stress drop after yield, and thus yielding, is caused by the nucleation of partial dislocations on the nonzero Schmid factor slip planes. We used the climbing image nudged elastic band (CINEB) method⁵³ to find the activation energy barrier $Q(\sigma, T)$ leading to the transition state between the reference state of interest and the final structure after yield, as illustrated in Figure S5. We note that a similar approach was used by Zhu et al. to calculate the activation energy barriers and nucleation stresses of pristine $\langle 100 \rangle$ -oriented Cu nanowires under compression.¹² The potential energy barrier $Q_0(\sigma)$ is calculated based on the energy difference between the initial equilibrium state and the saddle point along the minimum energy pathway. Figure S6 summarizes the activation energy barriers that must be crossed in order for yielding to occur at different stresses. It is clear that a transition in the activation energy–stress (Q_0 – σ) plot is observed, which happens around the transition stress for the change in incipient nucleation mechanism illustrated in Figure 3.

We then make the connection between nucleation stress, activation energy, and strain rate. Specifically, by converting the activation energy to strain rate using eq 2, we are able to determine the strain-rate-dependence of yield stress. To connect the activation energy $Q_0(\sigma)$ to strain rate, the two unknown parameters T_m and $\dot{\epsilon}_0$ in eq 2 should be estimated. We fit eq 2 to MD simulations at strain rates of 10^7 and 10^9 s⁻¹ using the activation energy barriers obtained by CINEB. In doing so, we find that $T_m = 940$ K and $\dot{\epsilon}_0 = 10^9$ s⁻¹ for silver bicrystalline nanowires with diameter of 4.5 nm. The values are comparable to the calculated surface disordering temperature of 926 K, where the surface melting temperature of [110] face is 0.75 of the bulk melting temperature⁵⁴ and an attempt factor of about 10^{10} s⁻¹.⁵⁵

After directly connecting activation energy to strain rate, we show in Figure 5 the resulting yield stress as a function of strain rate at 300 K for bicrystalline silver and copper nanowires with diameter of 4.5 nm. As can be seen in Figure 5a, there is a transition in the yield stress that occurs at a strain rate of about 10^2 s⁻¹ for bicrystalline silver nanowires with pristine surfaces, where an increased sensitivity to strain rate begins to manifest itself. A similar transition in the yield stress for bicrystalline copper nanowires with pristine surfaces is also observed as shown in Figure 5b, though at a slower strain rate as compared to silver, i.e., around 0.5 s⁻¹. The transition in yield stress for bicrystalline silver occurs at a higher strain rate than bicrystalline copper due to the fact that silver has a much lower SF energy, which corresponds to a lower energy barrier for defect nucleation, and thus a higher frequency of occurrence.

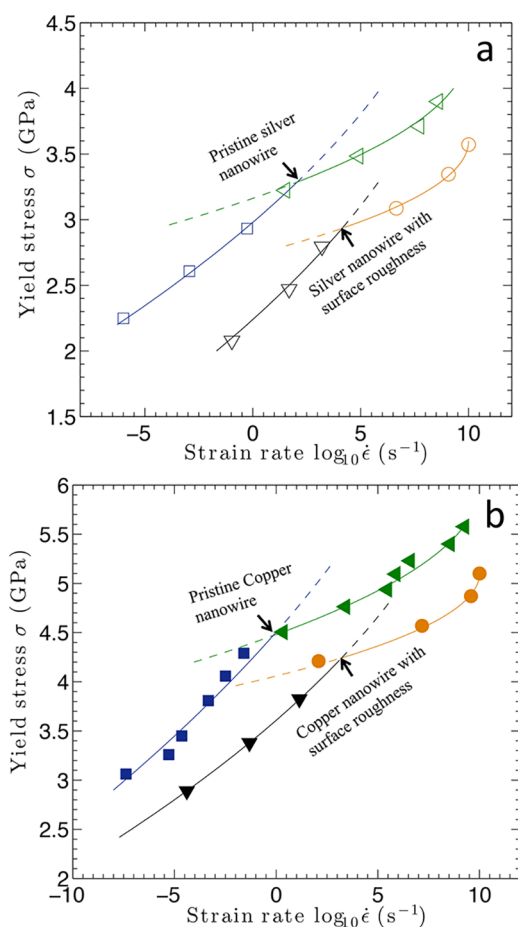


Figure 5. (a) Yield stress as a function of strain rate at room temperature for bicrystalline silver nanowires with diameter of 4.5 nm. The transition in yield stress occurs due to the different incipient nucleation mechanisms that occur at different stresses for the nanowires with pristine and rough surfaces as previously illustrated in Figure 3a and Figure S2a. (b) Yield stress as a function of strain rate at room temperature for bicrystalline copper nanowires with diameter of 4.5 nm. The transition in yield stress occurs due to the different incipient nucleation mechanisms that occur at different stresses in Figure 3b and Figure S2b.

While the existence of surface roughness did not impact the incipient nucleation mechanisms, the activation energy required for surface dislocation nucleation is reduced due to the presence of the surface roughness. The lower activation energy barrier for defect nucleation results in the yield stress transition being shifted to lower stress and higher strain rates for both the silver and copper bicrystalline nanowires. Specifically, the transition in the yield stress occurs at the higher strain rate of $10^4 s^{-1}$ for silver nanowires with surface roughness, and $10^3 s^{-1}$ for copper nanowires with surface roughness, as shown in Figure 5a,b. In contrast, the transition strain rate decreases with increasing nanowire diameter, due to the decreasing importance of surface effects. For example, the transition strain rate reduces to 1 and $10^3 s^{-1}$ for 6.5 nm bicrystalline silver nanowires with pristine and rough surfaces, respectively.

Figure 5 demonstrates that transitions in the strain-rate-dependent incipient nucleation events strongly impact the resulting yield stress for these bicrystalline nanowires. Furthermore, they demonstrate that the transition in the yield stress with strain rate is observed for the different materials even though the mechanisms governing the transition,

i.e., from partial dislocation slip on primary slip planes to the formation of long, planar SFs on non-Schmid slip planes in bicrystalline silver, to the formation of multiple TBs in bicrystalline copper, are different. They also illustrate the potential issues that can arise if the high stress nucleation mechanisms and stresses observed in MD simulations are directly extrapolated to experimental strain rates without directly observing any changes in incipient nucleation mechanism that can occur as the strain rate decreases.

Ductile-to-Brittle Transition at Experimental Strain Rates. We now discuss the effects of strain rate on the ductility and failure of the 4.5 nm diameter bicrystalline silver nanowires with surface roughness. To do so, we performed constant strain rate simulations using the SLME method at the high strain rate of $10^9 s^{-1}$, and a much slower strain rate of $10 s^{-1}$. As can be seen in Figure 6, when the strain rate decreases from 10^9 to 10

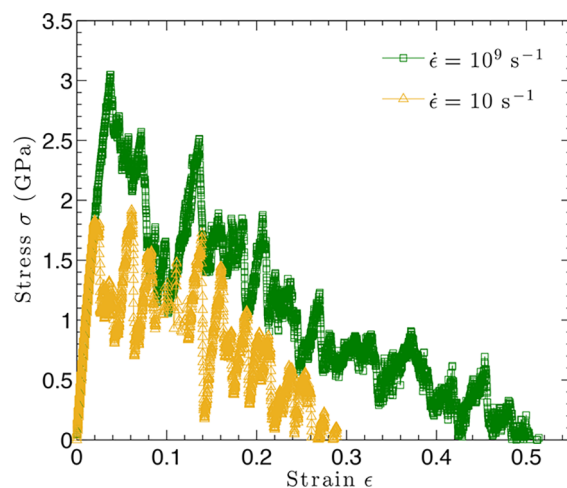


Figure 6. SLME simulated stress–strain curves for 4.5 nm bicrystalline silver nanowires with surface roughness at both MD-relevant ($\dot{\epsilon} = 10^9 s^{-1}$) and experimentally relevant ($\dot{\epsilon} = 10 s^{-1}$) strain rates.

s^{-1} , a significant reduction in fracture strain is observed, from 55% to 35% strain, which is similar to the ductile-to-brittle transition with decreasing strain rate observed experimentally by Ramachandramoorthy et al.²²

Figure 7 shows the deformation mechanisms leading to failure for the two different strain rates. For the high strain rate ($10^9 s^{-1}$) as shown in Figure 7a and Video S7, the nanowire yields at a strain of 4.1% due to the nucleation of leading partial dislocations primary slip planes (i.e., with nonzero Schmid factor). At a strain of 10%, more SFs are emitted from the GB in both grains, which induces GB migration along the nanowire length direction. As the strain increases, the nanowire eventually fractures at around 55% strain.

At the low, experimentally relevant strain rate ($10 s^{-1}$) as shown in Figure 7b and Video S8, the nanowire yields at around 2.5% strain. The yielding occurs due to the nucleation of partial dislocations on primary slip planes, but we also observe the presence of long, planar SFs on slip planes with zero Schmid factor, which represents the incipient nucleation event. The nucleation event of long, planar SFs on slip planes with zero Schmid factor preceding yielding by partial dislocations on primary slip planes is consistent with the predicted nucleation and yielding mechanisms shown in Figure S2b. As the strain increases, the surface roughness causes localization, and as such the onset of necking is observed

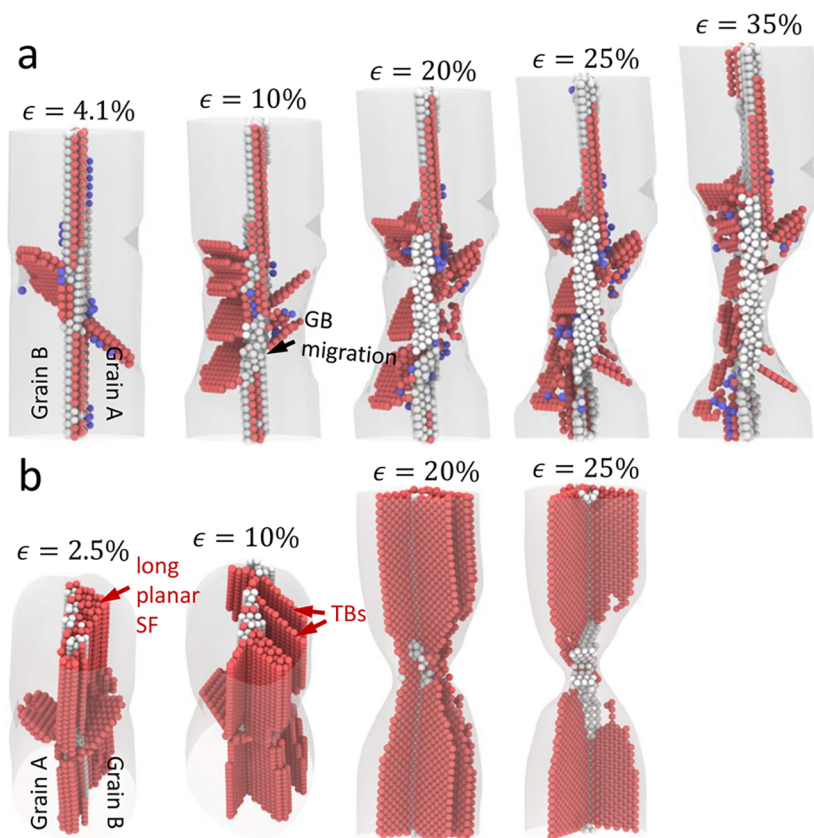


Figure 7. Atomic configurations showing the defect creation and evolution in 4.5 nm bicrystalline silver nanowires with surface roughness during tensile deformation at two strain rates of (a) 10^9 and (b) 10 s $^{-1}$. Only the GB and other planar defects are visualized. The following color convention is used: gray planes, GB; single red plane, TB; two adjacent red planes, SF.

around 5.5% strain, where we define necking to be the strain at which the cross sectional area begins, locally, to continuously decrease. As the strain increases, more planar defects are nucleated from the GB, and as a result, part of the GB is removed due to the nucleation of TBs at 10% strain. Furthermore, an obvious reduction in the cross sectional area at the necking region is observed at 20% strain. Fracture then occurs at 35% strain. The mechanisms governing the ductile-to-brittle transition are distinct from those recently reported for single-crystal silver nanowires by Zhong et al.⁵⁶ In that work, surface atom diffusion at slow strain rates was shown to lead to a brittle-to-ductile transition and superplasticity at slow strain rates. As this mechanism was not observed here, this suggests that defect nucleation from the GB controls the deformation characteristics of these bicrystalline metal nanowires.

There are several important differences in deformation mechanism as compared to the high strain rate MD simulations. First, instead of the formation of partial dislocations and SFs at high strain rates and small grains,²⁷ full dislocations are observed at the experimentally relevant strain rate, which is consistent with previous works demonstrating that planar defects along the nanowire axial direction can alter the deformation mode from twinning to full dislocations in metal nanopillars.⁵⁷ Specifically, as illustrated in Figure 7b, full dislocations become prevalent after the formation of TBs at the experimentally relevant strain rate. Similar behavior has been observed in MD simulations of $\langle 110 \rangle$ -oriented FCC metal nanopillars where twinning and SFs are the dominant deformation mechanisms in pristine nanopillars, while more full dislocations are observed in nanopillars

with a longitudinal TB.⁵⁷ The formation of full dislocations occurs because when two leading partials meet at the TB, a stair-rod dislocation forms and dissociates into two trailing partials, which eliminates the SFs produced by the leading partials. Second, very little GB migration is observed, which is different from the high strain rate simulations, and which limits the ductility of the nanowire at slow strain rates. This is because at the slower strain rate, more full dislocations are observed, while the dislocation nucleation is limited to the regions of both grains where the surface roughness is present.

We close with a final comparison to the experimental results of Ramachandramoorthy et al.²² Specifically, one indication that the ductile-to-brittle transition had occurred was a transition in plasticity behavior from distributed plasticity along the nanowire length, which delayed the eventual necking, to localized plasticity, leading to abrupt necking and brittle failure. While we observed distributed plasticity in the SLME simulations at high strain rates, it is possible that the defect density was not sufficiently large to also lead to the strain hardening that was observed experimentally. However, one reason for this may be that we did not consider the effects of pre-existing bulk and surface defects in the nanowires outside of the initial GB. As shown by Narayanan et al.,³² strain hardening can be observed in metallic nanowires by introducing pre-existing bulk and surface defects, which we have also observed in preliminary simulations of the bicrystalline metal nanowires.

Conclusions. In conclusion, we have demonstrated, using long time scale atomistic simulations, strain-rate-dependent transitions in both the incipient plastic deformation mechanism and yield stress in ultras-small bicrystalline copper and silver

nanowires. The simulations showed how the planar defects that nucleate from internal GB are impacted by strain rate. Specifically, the incipient nucleation mechanism was shown to transition from Shockley partials emitted on primary slip planes at high strain rates to the formation of planar defects on non-Schmid slip planes at experimental strain rates, where the incipient planar defect is the formation of multiple TBs for copper and SFs for silver. Finally, we demonstrate that, at experimental strain rates, a ductile-to-brittle transition in failure mode similar to previous experimental studies on bicrystalline silver nanowires is observed, which is driven by differences in dislocation activity and GB mobility as compared to the high strain rate case.

■ ASSOCIATED CONTENT

Supporting Information

The Supporting Information is available free of charge on the ACS Publications website at DOI: [10.1021/acs.nanolett.7b04972](https://doi.org/10.1021/acs.nanolett.7b04972).

Video S1: defect nucleation mechanisms up until yield of the Ag bicrystalline nanowire at a stress of 3.9 GPa using the SLME algorithm (AVI)

Video S2: defect nucleation mechanisms up until yield of the Ag bicrystalline nanowire at stress of 2.2 GPa using the SLME algorithm (AVI)

Video S3: defect nucleation mechanisms up until yield of the Cu bicrystalline nanowire at a stress of 5.23 GPa using the SLME algorithm (AVI)

Video S4: defect nucleation mechanisms up until yield of the Cu bicrystalline nanowire at stress of 4.29 GPa using the SLME algorithm (AVI)

Video S5: deformation mechanism to until yield of the Cu bicrystalline nanowire under tension at a slow strain rate ($\dot{\epsilon} = 10^{-1} \text{ s}^{-1}$) using the SLME algorithm (AVI)

Video S6: defect nucleation mechanisms up until yield of the Cu bicrystalline nanowire at stress of 4.29 GPa using the SLME algorithm (AVI)

Video S7: deformation mechanism to until failure of the Ag bicrystalline nanowire with surface roughness under tension at a high strain rate ($\dot{\epsilon} = 10^9 \text{ s}^{-1}$) using the SLME algorithm (AVI)

Video S8: deformation mechanism to until failure of the Ag bicrystalline nanowire with surface roughness under tension at a slow strain rate ($\dot{\epsilon} = 10 \text{ s}^{-1}$) using the SLME algorithm (AVI)

Video S9: deformation mechanism to until yield of the Cu bicrystalline nanowire under tension at a high strain rate ($\dot{\epsilon} = 10^9 \text{ s}^{-1}$) using classical MD (AVI)

Video S10: deformation mechanism to until yield of the Cu bicrystalline nanowire under tension at a high strain rate ($\dot{\epsilon} = 10^9 \text{ s}^{-1}$) using the SLME algorithm (AVI)

Surface roughness effect; size effect; ductile-to-brittle transition; and methodology used to perform the constant strain rate simulations, and calculate the activation energy and shear stress along slip direction (PDF)

■ AUTHOR INFORMATION

Corresponding Author

*E-mail: parkhs@bu.edu.

ORCID

Harold S. Park: [0000-0001-5365-7776](https://orcid.org/0000-0001-5365-7776)

Notes

The authors declare no competing financial interest.

■ ACKNOWLEDGMENTS

H.S.P. and W.W.T. gratefully acknowledge the support of the Mechanical Engineering department at Boston University. P.C. acknowledges financial support from the US Department of Energy under Grant DE-NE0008450. The authors declare no competing financial interests. All authors acknowledge the insightful comments of the reviewers.

■ REFERENCES

- (1) Xia, Y.; Yang, P.; Sun, Y.; Wu, Y.; Mayers, B.; Gates, B.; Yin, Y.; Kim, F.; Yan, H. *Adv. Mater.* **2003**, *15*, 353–389.
- (2) Barnes, W. L.; Dereux, A.; Ebbeson, T. W. *Nature* **2003**, *424*, 824–830.
- (3) Greer, J. R.; Hosson, J. T. M. D. *Prog. Mater. Sci.* **2011**, *56*, 654–724.
- (4) Park, H. S.; Cai, W.; Espinosa, H. D.; Huang, H. *MRS Bull.* **2009**, *34*, 178–183.
- (5) Weinberger, C. R.; Cai, W. *J. Mater. Chem.* **2012**, *22*, 3277–3292.
- (6) Wang, L.; Zhang, Z.; Han, X. *NPG Asia Mater.* **2013**, *5*, e40.
- (7) Zhu, Y. *Appl. Mech. Rev.* **2017**, *69*, 010802.
- (8) Diao, J.; Gall, K.; Dunn, M. L. *Nat. Mater.* **2003**, *2*, 656–660.
- (9) Park, H. S.; Gall, K.; Zimmerman, J. A. *Phys. Rev. Lett.* **2005**, *95*, 255504.
- (10) Liang, W.; Zhou, M.; Ke, F. *Nano Lett.* **2005**, *5*, 2039–2043.
- (11) Park, H. S.; Gall, K.; Zimmerman, J. A. *J. Mech. Phys. Solids* **2006**, *54*, 1862–1881.
- (12) Zhu, T.; Li, J.; Samanta, A.; Leach, A.; Gall, K. *Phys. Rev. Lett.* **2008**, *100*, 025502.
- (13) Greer, J. R.; Oliver, W. C.; Nix, W. D. *Acta Mater.* **2005**, *53*, 1821–1830.
- (14) Greer, J. R.; Nix, W. D. *Phys. Rev. B: Condens. Matter Mater. Phys.* **2006**, *73*, 245410.
- (15) Uchic, M. D.; Dimiduk, D. M.; Florando, J. N.; Nix, W. D. *Science* **2004**, *305*, 986–989.
- (16) Yue, Y.; Liu, P.; Zhang, Z.; Han, X.; Ma, E. *Nano Lett.* **2011**, *11*, 3151–3155.
- (17) Yue, Y.; Liu, P.; Deng, Q.; Ma, E.; Zhang, Z.; Han, X. *Nano Lett.* **2012**, *12*, 4045–4049.
- (18) Zheng, H.; Cao, A.; Weinberger, C. R.; Huang, J. Y.; Du, K.; Wang, J.; Ma, Y.; Xia, Y.; Mao, S. X. *Nat. Commun.* **2010**, *1*, 144.
- (19) Wang, L.; Teng, J.; Sha, X.; Zou, J.; Zhang, Z.; Han, X. *Nano Lett.* **2017**, *17*, 4733–4739.
- (20) Seo, J.-H.; Yoo, Y.; Park, N.-Y.; Yoon, S.-W.; Lee, H.; Han, S.; Lee, S.-W.; Seong, T.-Y.; Lee, S.-C.; Lee, K.-B.; Cha, P.-R.; Park, H. S.; Kim, B.; Ahn, J.-P. *Nano Lett.* **2011**, *11*, 3499–3502.
- (21) Seo, J.-H.; Park, H. S.; Yoo, Y.; Seong, T.-Y.; Li, J.; Ahn, J.-P.; Kim, B.; Choi, I.-S. *Nano Lett.* **2013**, *13*, S112–S116.
- (22) Ramachandramoorthy, R.; Gao, W.; Bernal, R.; Espinosa, H. *Nano Lett.* **2016**, *16*, 255–263.
- (23) Zhu, Y.; Qin, Q.; Xu, F.; Fan, F.; Ding, Y.; Zhang, T.; Wiley, B. J.; Wang, Z. L. *Phys. Rev. B: Condens. Matter Mater. Phys.* **2012**, *85*, 045443.
- (24) Yan, X.; Sharma, P. *Nano Lett.* **2016**, *16*, 3487–3492.
- (25) Yan, X.; Cao, P.; Tao, W.; Sharma, P.; Park, H. S. *J. Phys. D: Appl. Phys.* **2016**, *49*, 493002.
- (26) Wang, L.; Teng, J.; Liu, P.; Hirata, A.; Ma, E.; Zhang, Z.; Chen, M.; Han, X. *Nat. Commun.* **2014**, *5*, 4402.
- (27) Wang, L.; Han, X.; Liu, P.; Yue, Y.; Zhang, Z.; Ma, E. *Phys. Rev. Lett.* **2010**, *105*, 135501.
- (28) Jennings, A. T.; Li, J.; Greer, J. R. *Acta Mater.* **2011**, *59*, S627–S637.
- (29) Wang, J.; Huang, H. *Appl. Phys. Lett.* **2006**, *88*, 203112.
- (30) Deng, C.; Sansoz, F. *Nano Lett.* **2009**, *9*, 1517–1522.
- (31) Cao, A. J.; Wei, Y. G.; Mao, S. X. *Appl. Phys. Lett.* **2006**, *90*, 151909.

- (32) Narayanan, S.; Cheng, G.; Zeng, Z.; Zhu, Y.; Zhu, T. *Nano Lett.* **2015**, *15*, 4037–4044.
- (33) Cao, P.; Li, M.; Heugle, R. J.; Park, H. S.; Lin, X. *Phys. Rev. E* **2012**, *86*, 016710.
- (34) Cao, P.; Park, H. S.; Lin, X. *Phys. Rev. E* **2013**, *88*, 042404.
- (35) Cao, P.; Lin, X.; Park, H. S. *J. Mech. Phys. Solids* **2014**, *68*, 239–250.
- (36) Perez, D.; Uberuaga, B. P.; Voter, A. F. *Comput. Mater. Sci.* **2015**, *100*, 90–103.
- (37) Perez, D.; Uberuaga, B. P.; Shim, Y.; Amar, J. G.; Voter, A. F. *Annu. Rep. Comput. Chem.* **2009**, *5*, 79–98.
- (38) Voter, A. F.; Montalenti, F.; Germann, T. C. *Annu. Rev. Mater. Res.* **2002**, *32*, 321–346.
- (39) Kushima, A.; Lin, X.; Li, J.; Eapen, J.; Mauro, J. C.; Qian, X.; Diep, P.; Yip, S. *J. Chem. Phys.* **2009**, *130*, 224504.
- (40) Fan, Y.; Osetskiy, Y. N.; Yip, S.; Yildiz, B. *Proc. Natl. Acad. Sci. U. S. A.* **2013**, *110*, 17756–17761.
- (41) Fan, Y.; Kushima, A.; Yip, S.; Yildiz, B. *Phys. Rev. Lett.* **2011**, *106*, 125501.
- (42) Cao, P.; Short, M. P.; Yip, S. *Proc. Natl. Acad. Sci. U. S. A.* **2017**, *114* (52), 13631–13636.
- (43) Cao, P.; Yoon, G.; Tao, W.; Eom, K.; Park, H. S. *Sci. Rep.* **2015**, *5*, 8757.
- (44) Tao, W.; Yoon, G.; Cao, P.; Eom, K.; Park, H. S. *J. Chem. Phys.* **2015**, *143*, 125101.
- (45) Tschopp, M.; McDowell, D. *Philos. Mag.* **2007**, *87*, 3147–3173.
- (46) Zhang, L.; Lu, C.; Tieu, K. *Sci. Rep.* **2015**, *4*, 5919.
- (47) Mishin, Y.; Mehl, M.; Papaconstantopoulos, D.; Voter, A.; Kress, J. *Phys. Rev. B: Condens. Matter Mater. Phys.* **2001**, *63*, 224106.
- (48) Williams, P.; Mishin, Y.; Hamilton, J. *Modell. Simul. Mater. Sci. Eng.* **2006**, *14*, 817.
- (49) Stukowski, A. *Modell. Simul. Mater. Sci. Eng.* **2010**, *18*, 015012.
- (50) McDowell, M. T.; Leach, A. M.; Gall, K. *Nano Lett.* **2008**, *8*, 3613–3618.
- (51) Bernstein, N.; Tadmor, E. B. *Phys. Rev. B: Condens. Matter Mater. Phys.* **2004**, *69*, 094116.
- (52) Yamakov, V.; Wolf, D.; Salazar, M.; Phillpot, S.; Gleiter, H. *Acta Mater.* **2001**, *49*, 2713–2722.
- (53) Henkelman, G.; Uberuaga, B.; Jonsson, H. *J. Chem. Phys.* **2000**, *113*, 9901–9904.
- (54) Jayanthi, C.; Tosatti, E.; Pietronero, L. *Phys. Rev. B: Condens. Matter Mater. Phys.* **1985**, *31*, 3456.
- (55) Kobelev, N.; Kolyvanov, E.; Estrin, Y. *Acta Mater.* **2008**, *56*, 1473–1481.
- (56) Zhong, L.; Sansoz, F.; He, Y.; Wang, C.; Zhang, Z.; Mao, S. X. *Nat. Mater.* **2017**, *16*, 439–445.
- (57) Sainath, G.; Choudhary, B. *Phys. Lett. A* **2015**, *379*, 1902–1905.